catalysts

MDPI

Article

Nitrogen-Defect-Driven PtCu Dual-Atom Catalyst for Photocatalytic CO_2 Reduction

Xin He [1,2,3], Ting Liu [1,2,3], Hao Wang [1,2,3,*] and Yongming Luo [1,2,3,4,*]

[1] Faculty of Chemical Engineering, Kunming University of Science and Technology, Kunming 650500, China; 20222208059@stu.kust.edu.cn (X.H.); liuting1@stu.kust.edu.cn (T.L.)
[2] Key Laboratory of Yunnan Province for Synthesizing Sulfur-Containing Fine Chemicals, Kunming 650500, China
[3] The Innovation Team for Volatile Organic Compounds Pollutants Control and Resource Utilization of Yunnan Province, Kunming 650500, China
[4] Faculty of Environmental Science and Engineering, Kunming University of Science and Technology, Kunming 650500, China
* Correspondence: haowang668@kust.edu.cn (H.W.); environcatalysis@kust.edu.cn (Y.L.)

Abstract: Owing to global energy demands and climate change resulting from fossil fuel use, technologies capable of converting greenhouse gases into renewable energy resources are needed. One such technology is photocatalytic CO_2 reduction, which utilises solar energy to transform CO_2 into value-added hydrocarbons. However, the application of photocatalytic CO_2 reduction is limited by the inefficiency of existing photocatalysts. In this study, we developed a nitrogen-deficient g-C_3N_4-confined PtCu dual-atom catalyst (PtCu/V_N-C_3N_4) for photocatalytic CO_2 reduction. Aberration-corrected high-angle annular dark-field scanning transmission electron microscopy and X-ray absorption fine structure spectroscopy confirmed the atomic-level anchoring of PtCu pairs onto the nitrogen-vacancy-rich g-C_3N_4 nanosheets. The optimised PtCu/V_N-C_3N_4 exhibited superior photocatalytic performance, with CO and CH_4 evolution rates of 13.3 μmol/g/h and 2.5 μmol/g/h, respectively, under visible-light irradiation. Mechanistic investigations revealed that CO_2 molecules were preferentially adsorbed onto the PtCu dual sites, initiating a stepwise reduction pathway. In situ diffuse reflectance infrared Fourier-transform spectroscopy identified the formation of a key intermediate (HCOO*), whereas interfacial wettability studies demonstrated efficient H_2O adsorption on PtCu sites, providing essential proton sources for CO_2 protonation. Photoelectrochemical characterisation further confirmed the enhanced charge-transfer kinetics in PtCu/V_N-C_3N_4, which were attributed to the synergistic interplay between the nitrogen vacancies and dual-atom sites. Notably, the dual-active-site architecture minimised the competitive adsorption between CO_2 and H_2O molecules, thereby optimising the surface reaction pathways. This study establishes a rational strategy for designing atomically precise dual-atom catalysts through defect engineering, achieving concurrent improvements in activity, selectivity, and charge carrier utilisation for solar-driven CO_2 conversion.

Keywords: surface reaction mechanism; g-C_3N_4; nitrogen defects; PtCu dual-atom; photocatalytic CO_2 reduction

check for updates

Academic Editor: Jorge Bedia

Received: 27 April 2025
Revised: 18 May 2025
Accepted: 20 May 2025
Published: 4 June 2025

Citation: He, X.; Liu, T.; Wang, H.; Luo, Y. Nitrogen-Defect-Driven PtCu Dual-Atom Catalyst for Photocatalytic CO_2 Reduction. *Catalysts* **2025**, *15*, 558. https://doi.org/10.3390/catal15060558

Copyright: © 2025 by the authors. Licensee MDPI, Basel, Switzerland. This article is an open access article distributed under the terms and conditions of the Creative Commons Attribution (CC BY) license (https://creativecommons.org/licenses/by/4.0/).

1. Introduction

The dual challenges of escalating global energy demands and anthropogenic climate change driven by relentless fossil fuel consumption and consequent CO_2 emissions underscore the critical need for sustainable technologies capable of converting greenhouse gases into renewable energy resources [1,2]. Photocatalytic CO_2 reduction, a process that

utilises solar energy to transform CO_2 into value-added hydrocarbons (e.g., CO and CH_4), has emerged as a possible solution for addressing these intertwined crises. By simulating natural photosynthesis, this approach not only mitigates atmospheric CO_2 levels, but also produces storable chemical fuels, thereby closing the carbon cycle [3]. However, the practical implementation of this technology remains constrained by the inefficiency of existing photocatalysts, which are limited by inadequate photoabsorption, fast photogenerated charge–carrier recombination, and a lack of active sites for CO_2 activation and adsorption [4,5]. Among the various semiconductor materials explored, graphitic carbon nitride has attracted considerable interest because of its visible-light responsiveness, tuneable band structure, and robust thermal and chemical stabilities. Despite these advantages, the performance of pristine g-C_3N_4 is fundamentally limited by its narrow optical absorption spectrum (460 nm) and inefficient charge separation owing to the strong Coulombic interactions between the photogenerated electrons and holes. These intrinsic shortcomings necessitate innovative strategies for reengineering g-C_3N_4 at the atomic and electronic levels to unlock its full potential for solar-driven CO_2 conversion [6].

To overcome the limitations of conventional photocatalysts, recent advances have focused on defect engineering and atomic-scale metal incorporation to tailor the optical, electronic, and catalytic properties of the catalyst. Introducing nitrogen vacancies into g-C_3N_4 (denoted V_N-C_3N_4) represents a paradigm shift. These vacancies act as electron-deficient regions, creating mid-gap states that extend photoabsorption into the visible and near-infrared wavelengths, while simultaneously serving as electron traps to impede charge recombination. Furthermore, the undercoordinated carbon atoms adjacent to the vacancies can function as preferential anchoring sites for metal species, enhancing interfacial charge transfer. Parallel to defect engineering, the advent of dual-atom catalysts (DACs) has revolutionised heterogeneous catalysis by leveraging the synergistic interactions between adjacent metal sites [7,8]. DACs combine the multifunctional reactivity of bimetallic systems with the high atom-usage efficiency of single-atom catalysts, enabling precise control over reaction pathways. In this context, the strategic pairing of platinum (Pt) and copper (Cu) atoms offers a compelling synergy: Pt, with its strong CO_2 adsorption capability and low activation energy for C=O bond cleavage, complements the exceptional electron transfer kinetics and ability of Cu to stabilise key intermediates (e.g., *COOH and *CO). By immobilising PtCu dual atomic species on N-deficient g-C_3N_4, the resultant catalyst harmonises defect-mediated light harvesting with bimetallic cooperativity, creating a multifunctional platform for CO_2 reduction. This proposal not only optimises the adsorption-energy landscape for CO_2, but also establishes dual reaction centres to accelerate proton-coupled electron transfer, a rate-limiting step in photocatalytic CO_2 conversion [9].

Herein, we present a nitrogen-deficient g-C_3N_4-supported PtCu dual-atom catalyst (PtCu/V_N-C_3N_4) engineered for high-efficiency photocatalytic CO_2 reduction. This study not only establishes a blueprint for integrating defect engineering with dual-atom catalysis, but also elucidates the atomic-level interplay between vacancies and bimetallic sites, offering transformative insights for the rational design of photocatalysts. N-deficient g-C_3N_4 nanosheets were synthesised using a controlled alkali etching protocol, which selectively removed nitrogen atoms to generate vacancies while preserving the structural integrity of the material. This defect-rich framework not only broadened the photoabsorption edge to 620 nm, but also provided a high density of anchoring sites for the atomic-level dispersion of Pt and Cu. Through a codeposition strategy involving spatially confined reduction, Pt and Cu atoms were uniformly embedded in the N-deficient g-C_3N_4 lattice, forming stable PtN_X and CuN_X sites, as verified by the extended X-ray absorption fine structure (EXAFS). Aberration-corrected HAADF-STEM imaging further corroborated the atomic dispersion of PtCu diatoms, indicating direct metal–metal interactions. Under visible light ($\lambda > 420$ nm),

the optimised PtCu/V_N-C_3N_4 demonstrated a CO evolution rate of 13.3 μmol/g/h, which was three to five times faster than those of the majority of g-C_3N_4-based photocatalysts that have been reported. In situ diffuse reflectance infrared Fourier-transform spectroscopy (DRIFTS) revealed the reaction mechanism: dual-atom species preferentially adsorb and activate CO_2 molecules while stimulating the C=O bond to form *COOH intermediates, thus lowering the energy barrier for its protonation to *CO, which subsequently desorbs as CO.

2. Results and Discussion

A defect confinement strategy was employed to deposit the PtCu dual-atomic species on the V_N-C_3N_4 nanosheets. As illustrated in Figure S1, the surface of V_N-C_3N_4 exhibits a negative charge (zeta potential of −8.2 mV). The PtCu dual-atomic species and V_N-C_3N_4 nanosheets can form a solid interface more easily because of their opposing surface charges [10]. The morphology of the as-prepared PtCu/V_N-C_3N_4 composite was investigated using aberration-corrected transmission electron microscopy (AC-TEM). As shown in Figure 1a, the V_N-C_3N_4 exhibits a surface-exposed nanosheet structure, which provides an ideal environment for anchoring bimetallic Pt and Cu atomic sites. As shown in Figure 1b,c, the presence of uniformly distributed bright spots on the PtCu/V_N-C_3N_4 nanosheets indicates the homogeneous dispersion of Pt and Cu atoms across the nanosheet. Furthermore, the coexistence of Cu and Pt species was observed on the same nanosheets. This observation confirms that the PtCu obtained through the impregnation method exists in a dual-atomic configuration, rather than as isolated Cu and Pt NPs. Finally, as illustrated in Figure 1d, the homogeneous distribution of C, N, Cu, and Pt across the surface of the PtCu/V_N-C_3N_4 nanosheets was revealed by elemental mapping of the PtCu/V_N-C_3N_4 composite using energy-dispersive X-ray spectroscopy (EDS). The successful loading of PtCu onto the PtCu/V_N-C_3N_4 nanosheets was further confirmed by the corresponding high-angle annular dark-field scanning transmission electron microscopy (HAADF-STEM) images and quantitative elemental analysis presented in Figures S2 and S3.

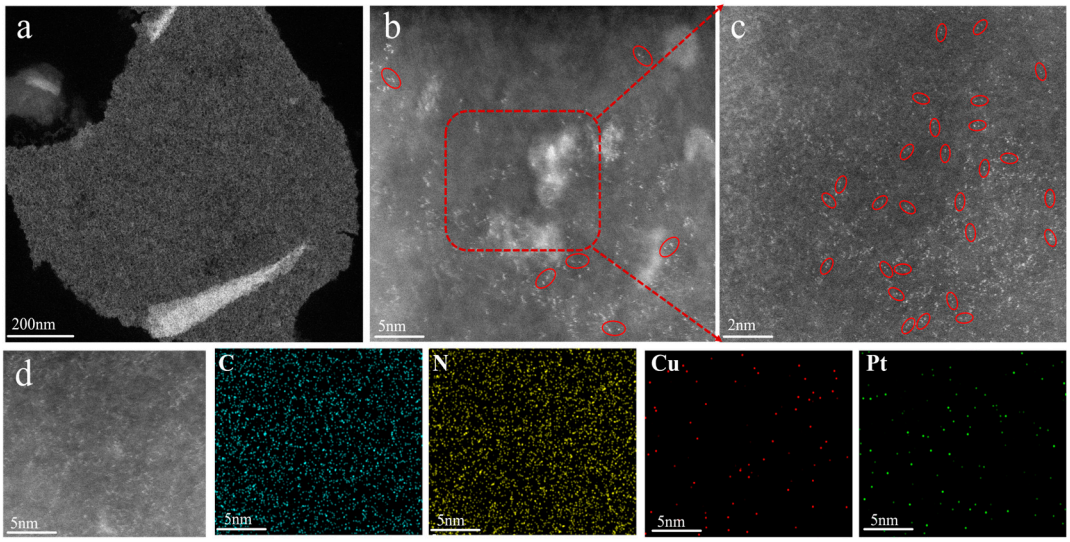


Figure 1. (**a**) HAADF-STEM image of V_N-C_3N_4 nanosheets, (**b**,**c**) HAADF-STEM images of PtCu/V_N-C_3N_4 observed at different scales, (**d**) EDS mapping of PtCu/V_N-C_3N_4.

The Fourier-transformation expanded X-ray-absorbing microstructure (FT EXAFS) was analysed in the R space for the determination of Pt and Cu atoms (Figure 2a,b). Referencing the standard Pt foil, the Pt L_3-edge k^3-weighted FT EXAFS of the PtCu/V_N-C_3N_4 sample exhibited a dominant peak at 1.57 Å, with no peaks corresponding to Pt–Pt

bonds (2.57 Å). This observation ruled out the formation of metallic crystalline Pt clusters or nanoparticles and confirmed the atomic dispersion of Pt [11]. Similarly, referencing the standard Cu foil, the PtCu/V_N-C_3N_4 sample displayed a dominant peak at 1.44 Å, with no peaks corresponding to Cu–Cu bonds. This excludes the formation of metallic crystalline Cu clusters or nanoparticles, confirming that Cu also exists in the atomic form [12]. These findings are consistent with the HAADF-STEM results. Furthermore, the existence of defects and the interaction between the PtCu dual-atomic species and V_N-C_3N_4 in the mixed specimen were studied by X-ray photoelectron spectroscopy (XPS). XPS (Figure S4) showed that the feature peaks in the PtCu/V_N-C_3N_4 specimens can be attributed to four elements: C, N, Pt, and Cu, suggesting that PtCu/V_N-C_3N_4 was successfully synthesised by defect confinement. XPS was performed on the as-prepared PtCu/V_N-C_3N_4 samples to investigate their elemental composition and valence states. The Cu 2p XPS profiles were separated into two peaks, as illustrated in Figure 2c. The peaks of Cu $2p_{3/2}$ and Cu $2p_{1/2}$ of Cu^{2+} in PtCu/V_N-C_3N_4 are found at 934.7 eV and 954.5 eV, respectively [13]. As illustrated in Figure 2d, decompressing the C 1s XPS spectrum into three peaks at 288.1 eV, 286.6 eV and 284.8 eV is possible, which correspond to NC=N, CNH_x, and sp^2 hybridised carbon (CC). The N 1s XPS spectrum can be matched with three peaks at 398.6 eV, 400.2 eV and 401.1 eV, as illustrated in Figure 2e, and these values are attributable to CN=C, $N(C)_3$, and CNH_x. The Pt 4f XPS spectrum exhibits two characteristic peaks at 73.09 eV and 76.19 eV, as illustrated in Figure 2f, and they are attributed to Pt $4f_{7/2}$ and Pt $4f_{5/2}$ of Pt4+ in PtCu/V_N-C_3N_4 [14].

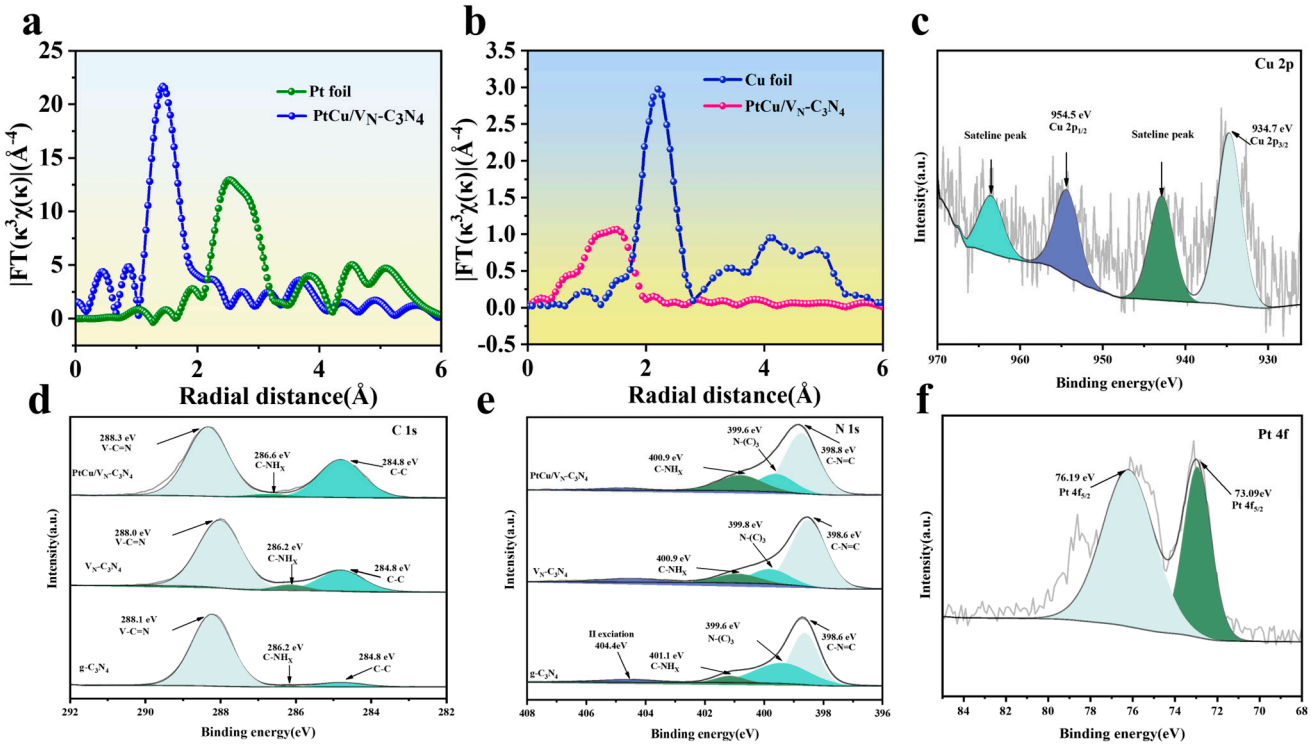


Figure 2. (**a**) The k^3-weighted Fourier-transformed Pt L_3-edge EXAFS spectra of PtCu/V_N-C_3N_4, Pt foil, (**b**) the k^3-weighted Fourier-transformed Cu L_3-edge EXAFS spectra of PtCu/V_N-C_3N_4, Cu foil, along with the fitting curve of PtCu/V_N-C_3N_4 in R-space, and the XPS spectra of (**c**) Cu 2p, (**d**) C 1s, (**e**) N 1s, and (**f**) Pt 4f.

Figure 3a shows the X-ray diffraction (XRD) patterns of the as-synthesised specimens. The samples exhibited similar crystalline structures. Two distinct diffraction peaks were observed in all specimens at approximately 12.7° (100) and 27.6° (002), which correspond to the in-plane repeating units of the conjugated aromatic system and the interlayer stacking

of g-C_3N_4, respectively [15]. Compared with g-C_3N_4, the (002) diffraction peak of V_N-C_3N_4 shows a slight leftward shift, indicating an increased interlayer distance according to Bragg's law $n\lambda = 2d\sin\theta$ [16]. However, no detectable diffraction peaks corresponding to Pt or Cu are observed for the PtCu/V_N-C_3N_4 composite, which may be attributed to their relatively low loading. Electron spin resonance (ESR) measurements conducted at room temperature (25 °C) on both g-C_3N_4 and V_N-C_3N_4 demonstrated that both samples exhibited a characteristic signal near g = 2.004 (Figure 3b), which was attributed to unpaired electrons in the heptazine rings [17–19]. Although both g-C_3N_4 and V_N-C_3N_4 possess carbon atoms with unpaired electrons within their heptazine ring structures, the successful incorporation of nitrogen vacancies into V_N-C_3N_4 induces the localisation of additional unpaired electrons on adjacent carbon atoms. This phenomenon was further substantiated by the significantly enhanced ESR signal intensity observed in V_N-C_3N_4 compared with that in g-C_3N_4. ESR spectroscopic analysis provided definitive evidence of the successful formation of nitrogen defects in V_N-C_3N_4. Furthermore, the stronger ESR signal of V_N-C_3N_4 indicated its enhanced electron delocalisation capability, thereby promoting a more efficient separation of the photogenerated charge carriers [20].

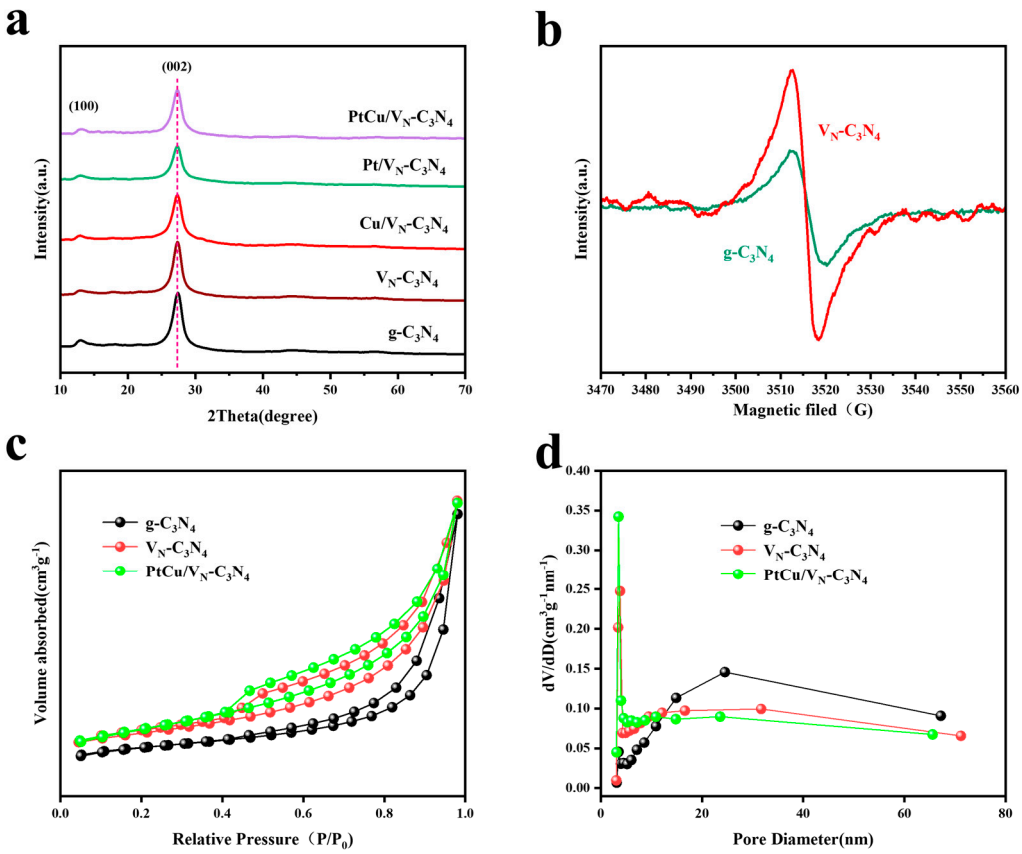


Figure 3. (**a**) XRD patterns of g-C_3N_4, V_N-C_3N_4, Pt/V_N-C_3N_4, Cu/V_N-C_3N_4, and PtCu/V_N-C_3N_4, (**b**) ESR, (**c**) N_2 adsorption–desorption, and (**d**) Barrett–Joyner–Halenda (BJH) pore size distribution plot.

The textural properties of the samples, including specific surface area and pore characteristics, were systematically investigated through N_2 adsorption–desorption measurements. As illustrated in Figure 3c, g-C_3N_4, V_N-C_3N_4, and PtCu/V_N-C_3N_4 exhibited characteristic Type IV isotherms with H3-type hysteresis loops, indicating the formation of a mesoporous structure [21]. The specific surface areas were determined to be 30.488, 56.906, and 63.825 $m^2\ g^{-1}$ for g-C_3N_4, V_N-C_3N_4, and PtCu/V_N-C_3N_4, respectively. The enhanced surface area provides an increased number of active sites for water molecule interactions, thereby improving photocatalytic activity. Furthermore, Barrett–Joyner–Halenda (BJH)

analysis revealed that PtCu/V_N-C_3N_4 possessed a pore size distribution ranging from 1 to 70 nm, with particularly abundant pores in the 10–20 nm range (Figure 3d). For a comparative analysis, the specific surface areas, pore volumes, and pore size distributions of g-C_3N_4, V_N-C_3N_4, and PtCu/V_N-C_3N_4 are summarised in Table S1 (Supporting Information).

The photocatalytic properties of CO_2 were tested using a mixed quartz glass reactor in a closed gas circulation system. Figure 4 illustrates the photocatalytic CO_2 reduction activity of all synthesised catalysts under simulated solar irradiation. Among them, PtCu/V_N-C_3N_4 demonstrated enhanced CO production, reaching up to 13.3 μmol/g/h after 4 h of irradiation, which is significantly higher than that of single-atom Pt/V_N-C_3N_4 (5.1 μmol/g/h), single-atom Cu/V_N-C_3N_4 (6.0 μmol/g/h), V_N-C_3N_4 (3.3 μmol/g/h) and g-C_3N_4 (2.2 μmol/g/h) (Figure 4a). Notably, the anchoring of single atoms (Pt or Cu) resulted in a relatively modest enhancement in CO production, approximately 1.5 and 2 times that of V_N-C_3N_4, respectively, whereas PtCu/V_N-C_3N_4 exhibited a CO production rate approximately 4.1 times that of V_N-C_3N_4 [22]. The results demonstrate that the synergistic effect induced by the incorporation of dual-atomic PtCu can significantly suppress photo-induced electron and hole recombination, thus increasing the photocatalytic CO_2 reduction activity. In addition, after five successive photocatalytic cycles (20 h), the PtCu/V_N-C_3N_4 complex showed a negligible decline in CO and CH_4 yields and strong cyclic stability under long illumination conditions (Figure 4b). Additionally, to systematically evaluate structural stability, the post-reaction PtCu/V_N-C_3N_4 catalyst was analysed by XRD. As shown in Figure 4c, the crystalline structure did not change after 20 h of reaction, indicating that PtCu/V_N-C_3N_4 exhibited a stable structure.

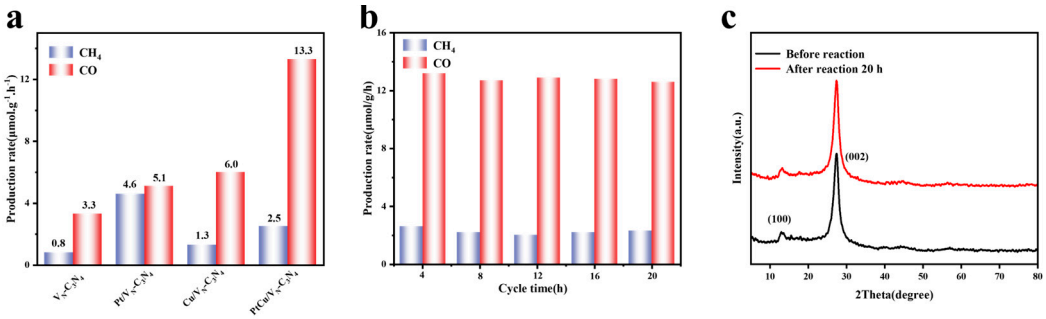


Figure 4. (**a**) The photocatalytic yields of CO and CH_4 and (**b**) cycling measurements of PtCu/V_N-C_3N_4 toward CO_2 photoreduction, and (**c**) XRD comparison before and after reaction.

The photocatalytic activity of semiconductor photocatalysts is predominantly governed by their capability to generate electron–hole pairs upon photoexcitation, which is fundamentally determined by the bandgap size and photo-absorption capacity of the semiconductor. As illustrated in Figure 5a, the composite photocatalyst (g-C_3N_4, V_N-C_3N_4, Pt/V_N-C_3N_4, Cu/V_N-C_3N_4, and PtCu/V_N-C_3N_4) was measured by diffusion reflectivity spectrometry (DRS). The g-C_3N_4 specimen exhibited an absorbing edge extending to 460 nm in the UV-visible region. In addition, the V_N-C_3N_4 sample exhibited a red-shifted absorption edge from 460 to 470 nm, accompanied by a broadened photoabsorption spectrum compared with that of g-C_3N_4 [23]. Notably, the Cu/V_N-C_3N_4, Pt/V_N-C_3N_4, and PtCu/V_N-C_3N_4 samples exhibited similar absorption edges. The respective bandgap energies, calculated using the Kubelka–Munk function, decreased from 2.76 eV to 2.58 eV (Figure 5b). These results suggest that a PtCu dual-atomic scheme can improve the photoabsorbing ability of the g-C_3N_4 defects. Notably, minimal shifts or even blue shifts were observed for the single-atom Pt/V_N-C_3N_4 and Cu/V_N-C_3N_4 samples. This observation suggests a synergistic effect between the Pt and Cu species, which optimises the photoabsorption properties of PtCu/V_N-C_3N_4, further confirming the successful preparation

of dual-atom PtCu. This observation suggests a synergistic effect between the Pt and Cu species, which optimises the photoabsorption properties of PtCu/V_N-C_3N_4, further confirming the successful preparation of dual-atomic Pt–Cu.

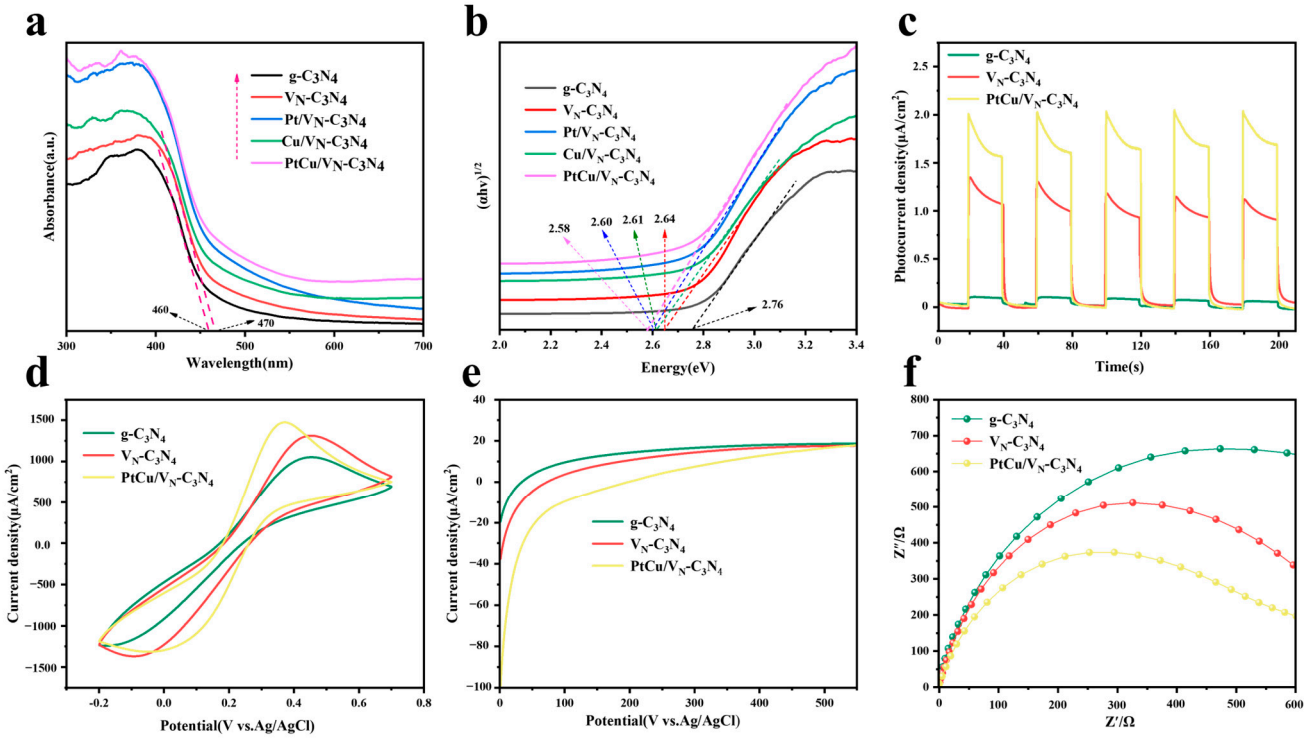


Figure 5. (**a**) UV–Vis DRS, (**b**) Tauc plots spectra of g-C_3N_4, V_N-C_3N_4 and PtCu/ V_N-C_3N_4, (**c**) transient photocurrent spectra, (**d**) CV, (**e**) LSV, and (**f**) EIS of g-C_3N_4, V_N-C_3N_4 and PtCu/V_N-C_3N_4 samples.

Through photoelectrochemistry, the ability to separate and migrate photogenerated electrons and holes was studied, which demonstrated that PtCu/V_N-C_3N_4 has excellent catalytic properties. Figure 5c shows the instantaneous photocurrent response curves of specimens subjected to intermittent radiation. In general, a positive relationship exists between the optical response strength and the electron–hole separation efficiency, which indicates improved photocatalysis. The experiment demonstrates that V_N-C_3N_4 has a photocurrent density approximately five times that of g-C_3N_4, which suggests an improvement in photogeneration owing to the introduction of defect energy levels. The maximum photocurrent strength of PtCu/V_N-C_3N_4 was higher than those of V_N-C_3N_4 and g-C_3N_4 [24]. In addition, Figure 5d shows the periodic cyclic voltammetry (CV) profile of the specimen, which shows clear anodising and cathodic peaks for every specimen. The current density achieved on PtCu/V_N-C_3N_4 is double or triple those of V_N-C_3N_4 and g-C_3N_4, suggesting that PtCu/V_N-C_3N_4 has a remarkable catalytic effect in increasing the efficiency of electron–hole pair separation. The overpotential of hydrogen evolution was studied using linear sweep voltammetry. As shown in Figure 5e, the PtCu/V_N-C_3N_4 sample exhibited the lowest hydrogen evolution overpotential compared with V_N-C_3N_4 and g-C_3N_4, providing strong evidence that PtCu/V_N-C_3N_4 more effectively supplied hydrogen sources for the CO_2 reduction process [25]. As illustrated in Figure 5f, the electrochemical impedance spectroscopy (EIS) results of these specimens demonstrate that the PtCu/V_N-C_3N_4 composite exhibits a lower resistance after the introduction of the PtCu dual-atomic species.

To further explain the mechanism for the improved photocatalytic properties of the PtCu/V_N-C_3N_4 composite, the behaviour of the photogenerated charges in the photocatalyst was investigated through photoluminescence (PL) spectroscopy [26]. The intensity

of the PL peak reflects the extent of electron–hole recombination, with a lower peak intensity indicating a reduced rate of electron–hole recombination. The PL spectra of g-C_3N_4, V_N-C_3N_4, Cu/V_N-C_3N_4, Pt/V_N-C_3N_4, and PtCu/V_N-C_3N_4 were recorded at an excitation wavelength of 300 nm. As illustrated in Figure S5, all samples exhibited similar peak shapes, with g-C_3N_4 demonstrating the highest peak intensity, indicating the most rapid electron–hole recombination rate among the samples. The peak intensity of V_N-C_3N_4 is significantly lower than that of g-C_3N_4, suggesting that the recombination of photogenerated charges in V_N-C_3N_4 is effectively suppressed. The PtCu/V_N-C_3N_4 sample exhibits the lowest peak intensity, indicating the highest charge-separation efficiency for the photogenerated carriers. In summary, the photochemical characterisation results suggest that the synergistic effect of PtCu dual-atomic species can accelerate the migration and transfer of photogenerated electrons, thereby enhancing the multifunctional photocatalytic conversion of CO_2 [27].

The water contact angles of g-C_3N_4 and V_N-C_3N_4 are 48.3°and 45.0°, respectively. Upon the introduction of PtCu atoms, the contact angle of PtCu/V_N-C_3N_4 decreased to 42.3° (Figure S6), indicating enhanced surface hydrophilicity, which facilitated the absorption of water and accelerated protonation reactions. The interaction of CO_2 molecules with the catalyst was studied by CO_2-TPD. As shown in Figure 6a, both PtCu/V_N-C_3N_4 and V_N-C_3N_4 exhibit a strong CO_2 desorption peak near 175 °C. However, for PtCu/V_N-C_3N_4, an enhanced CO_2 desorption peak appears at 450 °C as the temperature increases, which is attributed to the physical adsorption of CO_2 on the sample. In contrast, the CO_2 adsorption peak of V_N-C_3N_4 was weak and negligible [28]. The results indicate that, after loading PtCu dual-atom species, the multifunctional active sites on the surface of PtCu/V_N-C_3N_4 facilitate the adsorption of CO_2.

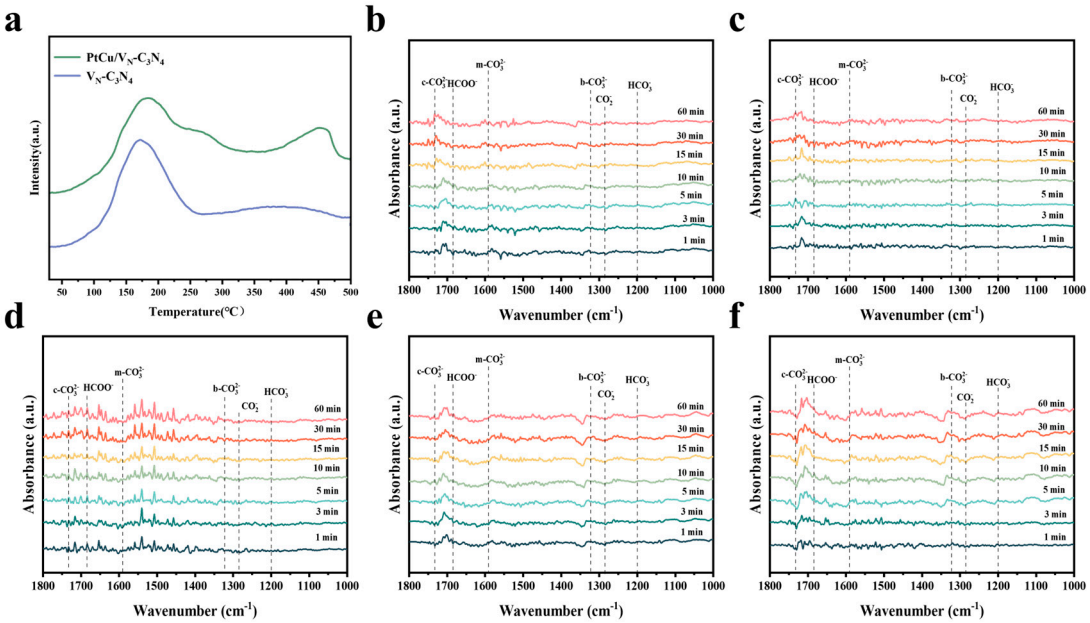


Figure 6. (**a**) CO_2-TPD of PtCu/V_N-C_3N_4, V_N-C_3N_4, in situ DRIFTS spectra of ultraviolet light irradiation (0–60 min), with wavenumber ranges of 1000–1800 cm^{-1} (**b**) g-C_3N_4, (**c**) V_N-C_3N_4, (**d**) Pt/V_N-C_3N_4, (**e**) Cu/V_N-C_3N_4, (**f**) PtCu/V_N-C_3N_4.

In situ DRIFTS spectroscopy revealed distinct characteristic vibrational signals corresponding to various intermediate species in the photocatalytic process. As illustrated in Figure 6b–f, CO^{2-} (1630 cm^{-1}), b-CO_3^{2-} (1599 cm^{-1}, 1325 cm^{-1}), and m-CO_3^{2-} (1514 cm^{-1}) exhibit negative signals [29]. The accumulation of these carbonate and carboxylate compounds over a long irradiation time (60 min) suggests that a significant intermediate $HCOO^-$ is formed, which is responsible for photocatalytic CO_2 conversion.

Furthermore, $HCOO^-$ acts as the rate-determining intermediate for the photocatalytic reduction of CO_2 to CO and CH_4 [30]. The subsequent consumption of $HCOO^-$ effectively participates in the photoreduction of CO_2, which is closely associated with the high selectivity toward methane and the remarkable reduction efficiency of CO_2. The results further corroborate the synergistic effect of the platinum–copper (PtCu) dual-active sites, which stabilise the $HCOO^-$ intermediate and facilitate its protonation to form *CO, thereby ultimately driving the selective formation of hydrocarbon products. In contrast, the DRIFTS peak strengths of the intermediates in the in situ DRIFTS of g-C_3N_4, Cu/V_N-C_3N_4, and Pt/V_N-C_3N_4 were significantly lower, indicating that their ability to convert CO_2 in the presence of light was inferior to that of PtCu/V_N-C_3N_4.

As shown in Figure 7, the introduced PtCu dual-atomic species exhibited a synergistic photocatalytic effect, where the dispersed Pt sites functioned as hydrogen storage centres participating in hydrogenation reactions, while Cu acted as an active adsorption centre for CO_2. Both active centres promoted long-lived charge separation. Research indicates that copper species have a strong binding effect on the surface adsorption CO_2 molecules by means of a strong hybridisation of Cu and the 2 p orbital of CO_2. During the photocatalytic process, evidence from the dynamic trajectories of the charge carriers highlights the synergistic oxidation facilitated by the dispersed PtCu active sites. The bimetallic PtCu atoms act as active centres, taking advantage of their respective strengths. On the other hand, the scattered PtCu atoms offer an active site for ultrafast photogeneration of electron transfer, thus maximising the lifetime of charge separation on the V_N-C_3N_4 nanosheets. The main reaction mechanism is as follows [31].

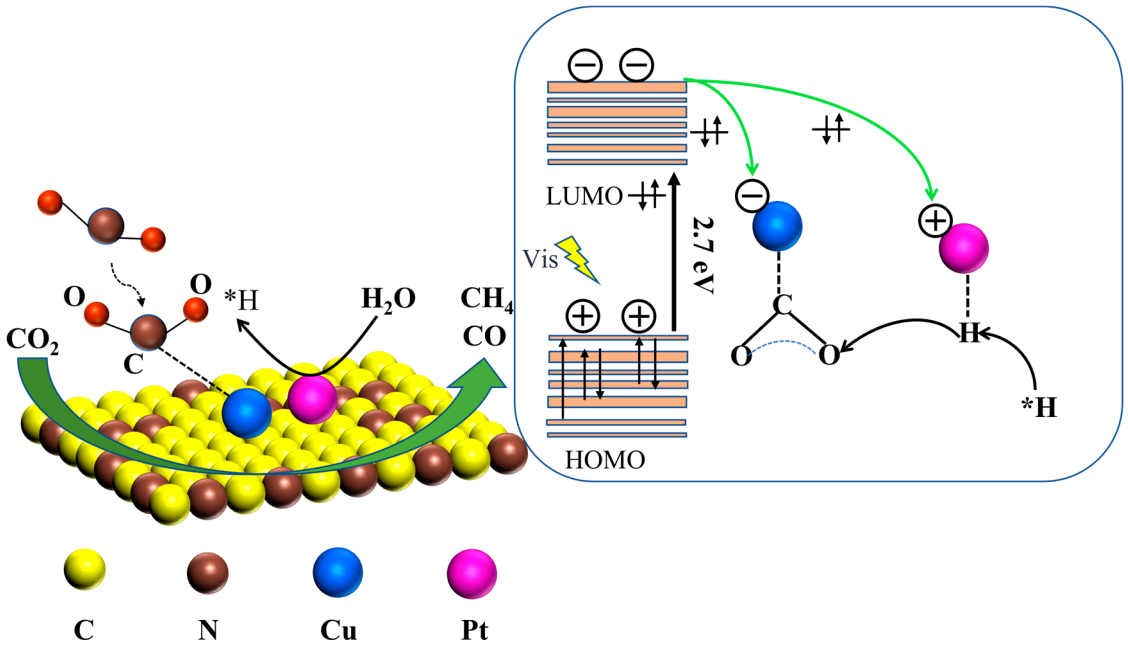


Figure 7. Schematic illustration of the photocatalytic CO_2 reduction mechanism on PtCu/V_N-C_3N_4.

CO_2 adsorption and activation:

$$CO_2 + \text{PtCu sites} \rightarrow CO_2^* \text{ (* denotes adsorbed species)} \quad (1)$$

Formation of HCOO* intermediate:

$$CO_2^* + H^+ + e^- \rightarrow HCOO^* \quad (2)$$

Protonation to *COOH:

$$HCOO^* + H^+ \rightarrow {}^*COOH \quad (3)$$

Reduction to CO:

$${}^*COOH + H^+ + e^- \rightarrow CO + H_2O \quad (4)$$

Further reduction to CH_4 (minor pathway):

$$CO + 6H^+ + 6e^- \rightarrow CH_4 + H_2O \quad (5)$$

3. Experimental Section

3.1. Chemicals

Melamine (AR, 99%), methanol (AR, 99%), absolute ethanol (AR, 99.5%), tetrabutylammonium hydroxide (AR, 40%), and ammonium sodium borohydride ($NaBH_4$, 98%) were obtained from the Sinopharm Chemical Reagent Co., Ltd. Copper chloride ($CuCl_2{\cdot}2H_2O$, $\geq$99.0%) and chloroplatinic acid hexahydrate ($H_2PtCl_6{\cdot}6H_2O$, Pt $\geq$ 37.5%) were sourced from the Shanghai Macklin Biochemical Technology Co., Ltd. In the present study, all chemical agents used were of analytical quality and used as obtained, with no further purification processes.

3.2. Synthesis of g-C_3N_4

Pure g-C_3N_4 was prepared via calcination. First, 5 g of melamine was placed in a 50 mL ceramic crucible, which was heated to 550 °C at 5 °C per minute, followed by a 3 h isothermal treatment [32]. After cooling naturally, the product was ground into a fine powder. The resulting yellow powder was dispersed in a mixed solvent containing methanol, ethanol, and tetrabutylammonium hydroxide, followed by magnetic stirring for 24 h and ultrasonication for 8 h. The finished product was separated by centrifugation, cleaned thoroughly with deionised water and alcohol, and dried for 12 h at 80 °C. The resulting yellow powder was crushed and collected for subsequent use.

3.3. Synthesis of Defect State g-C_3N_4 Nanosheets (V_N-C_3N_4)

The synthesis commenced with the homogeneous blending of melamine and sodium borohydride ($NaBH_4$) in an equimass ratio (100:1) through mechanical grinding. The thoroughly mixed composite was then loaded into an alumina crucible and subjected to controlled thermal treatment in a tube furnace. The temperature was accurately increased from the ambient temperature (20 °C) to 550 °C at a rate of 5 °C per minute and then subjected to isothermal annealing treatment for 3 h in a continuous stream of argon [33]. The samples were allowed to cool to room temperature naturally. The obtained yellow powder was mechanically crushed and dispersed in a ternary solvent system containing methanol, ethanol, and tetrabutylammonium hydroxide (volume ratio of 10:10:1). The mixture was subjected to continuous magnetic stirring for 24 h, followed by a 24 h ultrasonication treatment. The final product was isolated via centrifugation, thoroughly washed with deionised water, and dried overnight under ambient conditions. The resulting yellow powder was collected for further characterisation.

3.4. Synthesis of PtCu/V_N-C_3N_4

A PtCu/V_N-C_3N_4 composite catalyst was prepared using a wet impregnation method. First, aqueous solutions of $CuCl_2{\cdot}2H_2O$ and $H_2PtCl_6{\cdot}6H_2O$ with Cu and Pt mass concentrations of 10 mg/mL were prepared. Subsequently, a precisely weighed quantity of 0.1 g of V_N-C_3N_4 nanosheets was homogeneously dispersed in 30 mL of deionised water. Precisely

measured volumes of 0.267 mL of $CuCl_2 \cdot 2H_2O$ solution and 0.263 mL of $H_2PtCl_6 \cdot 6H_2O$ solution were sequentially introduced into the aforementioned dispersion. The resulting mixture was subjected to continuous magnetic stirring for 2 h and stilling for 24 h to facilitate the uniform adsorption of metal ions onto the surface of the V_N-C_3N_4 nanosheets. Finally, the powder was isolated by centrifugation, thoroughly washed with deionised water and anhydrous ethanol, and dried to obtain the PtCu/V_N-C_3N_4 photocatalyst. The synthesis of the PtCu/V_N-C_3N_4 photocatalyst is shown in Figure S7. Pt/V_N-C_3N_4 and Cu/V_N-C_3N_4 photocatalysts were prepared by the same method.

3.5. Characterisation

XRD images of the specimens were recorded in the 10–80° scanning range by means of a Bruker D8 Advance Apparatus with Cu Kα supply, working at 40 kV and 40 mA. The shapes and crystalline properties of the specimens were investigated using scanning electron microscopy (STEM, JEM-ARM 200p) and energy-dispersive X-ray spectrometry (EDS) (Bruker Xflash 5030) at an acceleration of 200 kV. The optical absorption characteristics were examined using UV-Vis DRS (UV2450 spectrophotometer, Cary 5000, Varian, USA) with $BaSO_4$ as the standard. An Escalab 250 apparatus (Escalab 250, Thermo Fisher, Waltham, USA) was used to analyse the specimen by means of XPS with a single-colour Al Kα irradiation source, and the C 1s peak binding energy was taken as a benchmark at 284.8 eV. The EPR (ESR) was measured with a JES-FA 200 spectrometer at 25 °C. A Zetasizer (Nano Z90, Malvern Instruments, Malvern City, United Kingdom) was used to measure the ζ-potential of the specimens.

3.6. Photocatalytic CO_2 Reduction Measurements

A Meery Change automated gas analyser (MC-SPB10) was employed to measure photocatalytic CO_2 reduction in H_2O. Using continuous mechanical agitation, 100 mg of catalyst, 100 mL of deionised water, and 100 µL of acetonitrile were used to create the catalyst system. A glass lid was used to seal the reaction container and to keep the system intact. Typically, the pressure inside the reactor is maintained below the normal value. Through the injection of cooling circulation water on the outside of the reactor, the reactor was kept at 6 °C. A gas chromatograph fitted with two detection systems was used to quantify the evolution of the gas: a heat conduction detector (TCD) and a flame ionisation detector (FID). Automatic sampling was carried out at 60 min intervals with a 5 A. Ultra-high purity argon (99.999%) was the carrier gas at a velocity of 20 mL/min. The GC was run with the injector held at 180 °C, the probe was kept at 360 °C, and the column was first set at 50 °C. Photocatalysis was performed using a 300 W xenon arc lamp (PLS-SXE300D, Beijing Perfect Light, Beijing, China) fitted with a 420 nm cut-off filter to provide 150 m W/cm^2 radiation.

3.7. Photoelectrochemical Test

Electrochemical characterisation, including transient photocurrent response spectroscopy, linear sweep voltammetry, the volt–ampere cycle method, and impedance spectroscopy, was performed using a conventional three-electrode configuration on a CHI660E electrochemical workstation (China). The electrochemical cell included a 0.5 M Na_2SO_4 aqueous electrolyte solution, with a platinum wire counter electrode and an Ag/AgCl reference electrode. The working electrode was fabricated by depositing the photocatalyst onto fluorine-doped tin oxide (FTO) conductive glass following the protocols established in our previous investigations. Photocurrent measurements were acquired under an applied bias of 0.5 V, with illumination provided by a 300 W Xe arc lamp. EIS was measured from 10^{-2} to 10^5 Hz, and the AC disturbance amplitude was 10 mV.

4. Conclusions

In summary, a new photocatalytic system was developed using a simple wet impregnation method to introduce PtCu atoms into nitrogen-deficient nanosheets. The PtCu dual-atomic species on the nitrogen-deficient carbon nitride nanosheets show synergy in the photocatalytic CO_2 reduction process, which facilitates tight interactions and quicker reaction dynamics. The synergistic action of the dual-atom metallic sites in PtCu/V_N-C_3N_4 not only combines the desired merits of Pt and Cu, but also accelerates the transport of photoproduced carriers in nitrogen-deficient carbon nitride nanosheets, thus improving the efficiency of CO_2 conversion. Furthermore, we demonstrated that the bimetallic PtCu atomic anchoring policy could decrease the loading of Pt while maintaining the maximum Pt mass activity. This new research holds significant importance for designing efficient photocatalytic materials with dispersed noble metals and improving effective atomic utilisation.

Supplementary Materials: The following supporting information can be downloaded at: https://www.mdpi.com/article/10.3390/catal15060558/s1. Figure S1. Zeta potential of V_N-C_3N_4. Figure S2. Quantitative elemental analysis of PtCu/V_N-C_3N_4. Figure S3. HAADF-STEM images of PtCu/V_N-C_3N_4. Figure S4. XPS survey spectrum. Figure S5. The PL spectrum for PtCu/V_N-C_3N_4, Cu/V_N-C_3N_4, Pt/V_N-C_3N_4, V_N-C_3N_4 and g-C_3N_4. Figure S6. Water contact angle tests of (a) g-C_3N_4, (b) V_N-C_3N_4, (c) PtCu/V_N-C_3N_4. Figure S7. Schematic illustration of the synthesis process for defective g-C_3N_4 and PtCu/V_N-C_3N_4 composite photocatalysts. Table S1. Basic parameters of N2 adsorption-desorption isotherms.

Author Contributions: Conceptualisation, H.W. and Y.L.; methodology, H.W.; software, T.L.; validation, X.H., T.L. and H.W.; formal analysis, X.H.; investigation, X.H.; resources, H.W. and Y.L.; data curation, X.H.; writing—original draft preparation, X.H.; writing—review and editing, X.H., T.L. and H.W.; visualisation, H.W.; supervision, H.W.; project administration, Y.L.; funding acquisition, Y.L. All authors have read and agreed to the published version of the manuscript.

Funding: This research was funded by the National Natural Science Foundation of China, grant number 42030712, National Key R&D Program of China, grant number 2023YFB3810803, Key Project of Natural Science Foundation of Yunnan Province, grant number No. 202101AS070026, Applied Basic Research Foundation of Yunnan Province, grant number 202401CF070105, and Kunming University of Science and Technology 'Double First-Class' Initiative Joint Special Fund—General Program, grant number 202301BE070001-016.

Data Availability Statement: The original contributions presented in this study are included in the article/Supplementary Material. Further inquiries can be directed to the corresponding author(s).

Acknowledgments: The author acknowledges the generous financial support from the National Natural Science Foundation of China (42030712), National Key R&D Program of China (2023YFB3810803), Key Project of Natural Science Foundation of Yunnan Province (No. 202101AS070026), Applied Basic Research Foundation of Yunnan Province (202401AS070650) and Kunming University of Science and Technology 'Double First-Class' Initiative Joint Special Fund—General Program (202301BE070001-016). Yunnan Major Scientific and Technological Projects (202302AG050002), and Yunnan Province Xingdian Talent Support Project (XDYC-YLXZ-2023-0004 and XDYC-YLXZ-2023-0004.

Conflicts of Interest: The authors declare no conflicts of interest.

References

1. Li, X.; Li, N.; Gao, Y.; Ge, L. Design and Applications of Hollow-Structured Nanomaterials for Photocatalytic H_2 Evolution and CO_2 Reduction. *Chin. J. Catal.* **2022**, *43*, 679–707. [CrossRef]
2. Jiang, J.; Li, F.; Su, H.; Gao, Y.; Li, N.; Ge, L. Flower-like $NiCo_2S_4$/NiFeP/NF Composite Material as an Effective Electrocatalyst with High Overall Water Splitting Performance. *Chin. Chem. Lett.* **2022**, *33*, 4367–4374. [CrossRef]

3. Qiu, S.; Shen, Y.; Wei, G.; Yao, S.; Xi, W.; Shu, M.; Si, R.; Zhang, M.; Zhu, J.; An, C. Carbon Dots Decorated Ultrathin CdS Nanosheets Enabling In-Situ Anchored Pt Single Atoms: A Highly Efficient Solar-Driven Photocatalyst for Hydrogen Evolution. *Appl. Catal. B Environ.* **2019**, *259*, 118036. [CrossRef]
4. Han, B.; Guo, Y.; Huang, Y.; Xi, W.; Xu, J.; Luo, J.; Qi, H.; Ren, Y.; Liu, X.; Qiao, B.; et al. Strong Metal–Support Interactions between Pt Single Atoms and TiO_2. *Angew. Chem. Int. Ed.* **2020**, *59*, 11824–11829. [CrossRef]
5. Liu, L.; Hu, T.; Dai, K.; Zhang, J.; Liang, C. A Novel Step-Scheme $BiVO_4/Ag_3VO_4$ Photocatalyst for Enhanced Photocatalytic Degradation Activity under Visible Light Irradiation. *Chin. J. Catal.* **2021**, *42*, 46–55. [CrossRef]
6. Li, Y.; Zhou, M.; Cheng, B.; Shao, Y. Recent Advances in g-C_3N_4-Based Heterojunction Photocatalysts. *J. Mater. Sci. Technol.* **2020**, *56*, 1–17. [CrossRef]
7. Bi, L.; Liang, X.; Zhang, L.; Xie, T. The Study of Photogenerated Charge Behavior and Photocatalytic Hydrogen Evolution on g-C_3N_4 Decorated with PtCox Bimetal. *J. Alloys Compd.* **2021**, *853*, 156843. [CrossRef]
8. Liu, X.; Chen, M.; Zhang, X. Halogen Anions (F^-, Cl^-, Br^-) Modulated the Localized Microstructure of g-C_3N_4 to Facilitate Charge Separation and Transport and Enhance Photocatalytic Activities. *Catal. Sci. Technol.* **2024**, *14*, 4036–4044. [CrossRef]
9. Nagar, O.P.; Barman, T.; Marumoto, K.; Shimoi, Y.; Matsuishi, K.; Chouhan, N. Metal Free S-Scheme Heterojunction S-Doped g-C_3N_4/g-C_3N_4 for Enhanced Photocatalytic Water Splitting. *Int. J. Hydrogen Energy* **2024**, *87*, 526–538. [CrossRef]
10. Wang, H.; Wang, X.; Hu, P.; Liu, T.; Weng, B.; Ye, K.; Luo, Y.; Ji, H. Vacancy Pair Induced Surface Chemistry Reconstruction of $Cs_2AgBiBr_6/Bi_2WO_6$ Heterojunction to Enhance Photocatalytic CO_2 Reduction. *Appl. Catal. B Environ. Energy* **2024**, *351*, 123956. [CrossRef]
11. Shi, X.; Huang, Y.; Bo, Y.; Duan, D.; Wang, Z.; Cao, J.; Zhu, G.; Ho, W.; Wang, L.; Huang, T.; et al. Highly Selective Photocatalytic CO_2 Methanation with Water Vapor on Single-Atom Platinum-Decorated Defective Carbon Nitride. *Angew. Chem. Int. Ed.* **2022**, *61*, e202203063. [CrossRef] [PubMed]
12. Jiang, Z.; Sun, W.; Shang, H.; Chen, W.; Sun, T.; Li, H.; Dong, J.; Zhou, J.; Li, Z.; Wang, Y.; et al. Atomic Interface Effect of a Single Atom Copper Catalyst for Enhanced Oxygen Reduction Reactions. *Energy Environ. Sci.* **2019**, *12*, 3508–3514. [CrossRef]
13. Zhang, Y.; Chen, F.; Yang, X.; Guo, Y.; Zhang, X.; Dong, H.; Wang, W.; Lu, F.; Lu, Z.; Liu, H.; et al. Electronic Metal-Support Interaction Modulates Cu Electronic Structures for CO_2 Electroreduction to Desired Products. *Nat. Commun.* **2025**, *16*, 1956. [CrossRef]
14. Zhao, Y.; Liu, P.; Liu, W.; Lv, H.; Peng, Z.; Han, C.; Tian, J.; Ye, F.; Cheng, Z.; Huang, Y. AuPt Bimetallic Loaded Defect State g-C_3N_4 Enhances Photocatalytic H_2 Evolution: Exploring Synergistic Effects and Charge Transfer Mechanisms. *Sep. Purif. Technol.* **2025**, *354*, 128884. [CrossRef]
15. Song, H.; Liu, L.; Wang, H.; Feng, B.; Xiao, M.; Tang, Y.; Qu, X.; Gai, H.; Huang, T. Adjustment of the Band Gap of Co-Doped KCl/NH_4Cl/g-C_3N_4 for Enhanced Photocatalytic Performance under Visible Light. *Mater. Sci. Semicond. Process.* **2021**, *128*, 105757. [CrossRef]
16. Zhang, D.; Guo, Y.; Zhao, Z. Porous Defect-Modified Graphitic Carbon Nitride via a Facile One-Step Approach with Significantly Enhanced Photocatalytic Hydrogen Evolution under Visible Light Irradiation. *Appl. Catal. B Environ.* **2018**, *226*, 1–9. [CrossRef]
17. Li, S.; Dong, G.; Hailili, R.; Yang, L.; Li, Y.; Wang, F.; Zeng, Y.; Wang, C. Effective Photocatalytic H_2O_2 Production under Visible Light Irradiation at g-C_3N_4 Modulated by Carbon Vacancies. *Appl. Catal. B Environ.* **2016**, *190*, 26–35. [CrossRef]
18. Rao, F.; Zhong, J.; Li, J. Improved Visible Light Responsive Photocatalytic Hydrogen Production over g-C_3N_4 with Rich Carbon Vacancies. *Ceram. Int.* **2022**, *48*, 1439–1445. [CrossRef]
19. Xie, L.; Lu, D.; Kondamareddy, K.K.; Ho, W.; Wu, Q.; Zeng, Y.; Zhang, Y.; Wang, Z.; Zhao, B.; Li, J.; et al. Interfacial Optimization of Oxygen-Vacancy-Induced 1D/2D CeO_2 Nanotubes/g-C_3N_4 Step-Scheme Heterojunction with Enhanced Visible-Light Photocatalysis and Mechanism Insight. *J. Alloys Compd.* **2022**, *923*, 166330. [CrossRef]
20. Liang, Q.; Li, Z.; Huang, Z.; Kang, F.; Yang, Q. Holey Graphitic Carbon Nitride Nanosheets with Carbon Vacancies for Highly Improved Photocatalytic Hydrogen Production. *Adv. Funct. Mater.* **2015**, *25*, 6885–6892. [CrossRef]
21. He, F.; Chen, G.; Yu, Y.; Zhou, Y.; Zheng, Y.; Hao, S. The Sulfur-Bubble Template-Mediated Synthesis of Uniform Porous g-C_3N_4 with Superior Photocatalytic Performance. *Chem. Commun.* **2015**, *51*, 425–427. [CrossRef] [PubMed]
22. Ma, X.; Chen, Q.; Han, C.; Zhou, S.; Li, Z.; Liu, J.; Hu, F.; Wang, J.; Wang, N.; Zhu, Y.; et al. Synergistic Optimization of Morphology and Vacancies on Diatomic Rhodium Catalysts Dispersed on Carbon Nitride for Efficient Photocatalytic Reduction of CO_2. *Adv. Funct. Mater.* **2024**, *34*, 2307733. [CrossRef]
23. Lin, F.; Wang, T.; Ren, Z.; Cai, X.; Wang, Y.; Chen, J.; Wang, J.; Zang, S.; Mao, F.; Lv, L. Central Nitrogen Vacancies in Polymeric Carbon Nitride for Boosted Photocatalytic H_2O_2 Production. *J. Colloid. Interface Sci.* **2023**, *636*, 223–229. [CrossRef]
24. Yuan, H.; Du, J.; Ming, M.; Chen, Y.; Jiang, L.; Han, Z. Combination of Organic Dye and Iron for CO_2 Reduction with Pentanuclear Fe_2Na_3 Purpurin Photocatalysts. *J. Am. Chem. Soc.* **2022**, *144*, 4305–4309. [CrossRef] [PubMed]
25. Yang, H.; Zhang, D.; Luo, Y.; Yang, W.; Zhan, X.; Yang, W.; Hou, H. Highly Efficient and Selective Visible-Light Driven Photoreduction of CO_2 to CO by Metal–Organic Frameworks-Derived Ni@Co@O Porous Microrods. *Small* **2022**, *18*, 2202939. [CrossRef]

26. Zhang, J.; Dang, Y.; Wang, W.; Zhan, H.; Song, X.; Ma, B. Efficiently Improving the Photocatalytic Hydrogen Evolution of g-C_3N_4 by (Pt/MoP) Composite Co-Catalyst with Low Amount of Pt. *Int. J. Hydrogen Energy* **2022**, *47*, 2338–2346. [CrossRef]
27. Wang, Y.; Zhao, J.; Liu, Y.; Liu, G.; Ding, S.; Li, Y.; Xia, J.; Li, H. Synergy between Plasmonic and Sites on Gold Nanoparticle-Modified Bismuth-Rich Bismuth Oxybromide Nanotubes for the Efficient Photocatalytic C C Coupling Synthesis of Ethane. *J. Colloid. Interface Sci.* **2022**, *616*, 649–658. [CrossRef]
28. Zhang, M.; Mao, Y.; Bao, X.; Zhai, G.; Xiao, D.; Liu, D.; Wang, P.; Cheng, H.; Liu, Y.; Zheng, Z.; et al. Coupling Benzylamine Oxidation with CO_2 Photoconversion to Ethanol over a Black Phosphorus and Bismuth Tungstate S-Scheme Heterojunction. *Angew. Chem.* **2023**, *135*, e202302919. [CrossRef]
29. Wang, M.; Shen, M.; Jin, X.; Tian, J.; Li, M.; Zhou, Y.; Zhang, L.; Li, Y.; Shi, J. Oxygen Vacancy Generation and Stabilization in CeO_{2-x} by Cu Introduction with Improved CO_2 Photocatalytic Reduction Activity. *ACS Catal.* **2019**, *9*, 4573–4581. [CrossRef]
30. Liu, X.; Ye, M.; Zhang, S.; Huang, G.; Li, C.; Yu, J.; Wong, P.K.; Liu, S. Enhanced Photocatalytic CO_2 Valorization over TiO_2 Hollow Microspheres by Synergetic Surface Tailoring and Au Decoration. *J. Mater. Chem. A* **2018**, *6*, 24245–24255. [CrossRef]
31. Cheng, L.; Zhang, P.; Wen, Q.; Fan, J.; Xiang, Q. Copper and Platinum Dual-Single-Atoms Supported on Crystalline Graphitic Carbon Nitride for Enhanced Photocatalytic CO_2 Reduction. *Chin. J. Catal.* **2022**, *43*, 451–460. [CrossRef]
32. Wei, D.; Wu, J.; Wang, Y.; Zhong, J.; Li, D.; Jin, X.; Wu, Y.; Chen, P.; Liu, H.; Lv, W.; et al. Dual Defect Sites of Nitrogen Vacancy and Cyano Group Synergistically Boost the Activation of Oxygen Molecules for Efficient Photocatalytic Decontamination. *Chem. Eng. J.* **2023**, *462*, 142291. [CrossRef]
33. Lin, H.; Tang, X.; Wang, J.; Zeng, Q.; Chen, H.; Ren, W.; Sun, J.; Zhang, H. Enhanced Visible-Light Photocatalysis of Clofibric Acid Using Graphitic Carbon Nitride Modified by Cerium Oxide Nanoparticles. *J. Hazard. Mater.* **2021**, *405*, 124204. [CrossRef] [PubMed]

Disclaimer/Publisher's Note: The statements, opinions and data contained in all publications are solely those of the individual author(s) and contributor(s) and not of MDPI and/or the editor(s). MDPI and/or the editor(s) disclaim responsibility for any injury to people or property resulting from any ideas, methods, instructions or products referred to in the content.